A photoactivable multi-inhibitor nanoliposome for tumour control and simultaneous inhibition of treatment escape pathways

Q1

Bryan Q. Spring[1,2†], R. Bryan Sears[1,3†], Lei Zak Zheng[1†], Zhiming Mai[1], Reika Watanabe[4], Margaret E. Sherwood[1], David A. Schoenfeld[5], Brian W. Pogue[6], Stephen P. Pereira[7], Elizabeth Villa[4] and Tayyaba Hasan[1,8]*

Nanoscale drug delivery vehicles can facilitate multimodal therapies of cancer by promoting tumour-selective drug release. However, few are effective because cancer cells develop ways to resist and evade treatment. Here, we introduce a photoactivable multi-inhibitor nanoliposome (PMIL) that imparts light-induced cytotoxicity in synchrony with a photoinitiated and sustained release of inhibitors that suppress tumour regrowth and treatment escape signalling pathways. The PMIL consists of a nanoliposome doped with a photoactivable chromophore (benzoporphyrin derivative, BPD) in the lipid bilayer, and a nanoparticle containing cabozantinib (XL184)—a multikinase inhibitor—encapsulated inside. Near-infrared tumour irradiation, following intravenous PMIL administration, triggers photodynamic damage of tumour cells and microvessels, and simultaneously initiates release of XL184 inside the tumour. A single PMIL treatment achieves prolonged tumour reduction in two mouse models and suppresses metastatic escape in an orthotopic pancreatic tumour model. The PMIL offers new prospects for cancer therapy by enabling spatiotemporal control of drug release while reducing systemic drug exposure and associated toxicities.

Nanoscale drug delivery systems enable controlled drug release with increased tumour selectivity and reduced toxicity[1]. Recently, multifunctional nanoparticles activated by external stimuli have emerged to enhance tumour-selective drug release[1]. These activable delivery vehicles include optically responsive nanomaterials that support a broad range of biophotonic therapy and imaging applications[2–4], offering great promise for facilitating multimodal therapies of cancer. However, a fundamental challenge in oncology is that a number of resistance mechanisms and escape pathways ultimately limit treatment efficacy[5,6].

Here, we report near-infrared (NIR) light-activated PMILs that impart photocytotoxicity to multiple tumour compartments and enable photoinitiated, sustained release of a multimolecular inhibitor with potent antiangiogenic activity and suppression of prominent treatment escape pathways (Fig. 1a). This unique approach impairs multiple, distinct molecular targets and is motivated by a three-way mechanistic interaction to combine: (i) photodynamic therapy (PDT)-induced tumour cell apoptotic signalling with XL184 inhibition of anti-apoptotic signalling pathways that promote cell survival; (ii) PDT-induced microvessel damage with sustained XL184 inhibition of vascular endothelial growth factor (VEGF) signalling to suppress tumour angiogenesis and vascular regrowth; and (iii) exploiting a second molecular target of XL184, sustained inhibition of MET—the receptor tyrosine kinase for hepatocyte growth factor—signalling to suppress cancer cell motility, invasion and metastatic escape in response to tumour hypoxia

induced by vascular damage and antiangiogenic therapy[7,8]. We show that BPD–XL184 PMILs realize these complementary interactions, resulting in enhanced tumour reduction *in vivo* in two mouse models of human pancreatic ductal adenocarcinoma (PDAC). In contrast to the corresponding monotherapies and combination therapy using conventional drug formulations, a single treatment cycle using PMILs results in prolonged local tumour control in a subcutaneous and in an orthotopic PDAC mouse model.

VEGF and MET are prime examples of tumour signalling pathways that promote treatment escape. VEGF and its receptors (for example VEGFR2) represent key targets for antiangiogenic therapy, and upregulation of VEGF signalling has been observed in response to radiotherapy[9], chemotherapy[10], cytoreductive surgery[11] and PDT[12,13]. MET is frequently expressed by cancer stem-like cells thought to drive tumour recurrence[14], and abnormal MET signalling has been shown to promote the epithelial–mesenchymal transition[15], cancer cell stemness[15] as well as tumour growth, invasion and metastasis[5,15]. Moreover, MET signalling is also observed in response to anti-VEGF therapy and comprises a prominent escape mechanism from antiangiogenic treatments[5]. When the tumour vasculature is pruned by anti-VEGF therapy, the hypoxic tumour microenvironment stimulates MET expression[7,8,16]. McDonald and colleagues elegantly demonstrated that concurrent inhibition of the VEGF and MET signalling pathways results in the favourable benefits of antiangiogenic therapy in slowing

[1]Wellman Center for Photomedicine, Massachusetts General Hospital and Harvard Medical School, Boston, Massachusetts 02114, USA. [2]Department of Physics, Northeastern University, Boston, Massachusetts 02115, USA. [3]Department of Chemistry, Emmanuel College, Boston, Massachusetts 02115, USA. [4]Department of Chemistry and Biochemistry, University of California San Diego, La Jolla, California 92093, USA. [5]Massachusetts General Hospital and Harvard University, Biostatistics Unit, Boston, Massachusetts 02114, USA. [6]Thayer School of Engineering, Dartmouth College, Hanover, New Hampshire 03755, USA. [7]UCL Institute for Liver and Digestive Health, University College London, Royal Free Hospital Campus, London NW3 2QG, UK. [8]Division of Health Sciences and Technology, Harvard University and Massachusetts Institute of Technology, Cambridge, Massachusetts 02139, USA. [†]These authors contributed equally to this work. *e-mail: thasan@mgh.harvard.edu
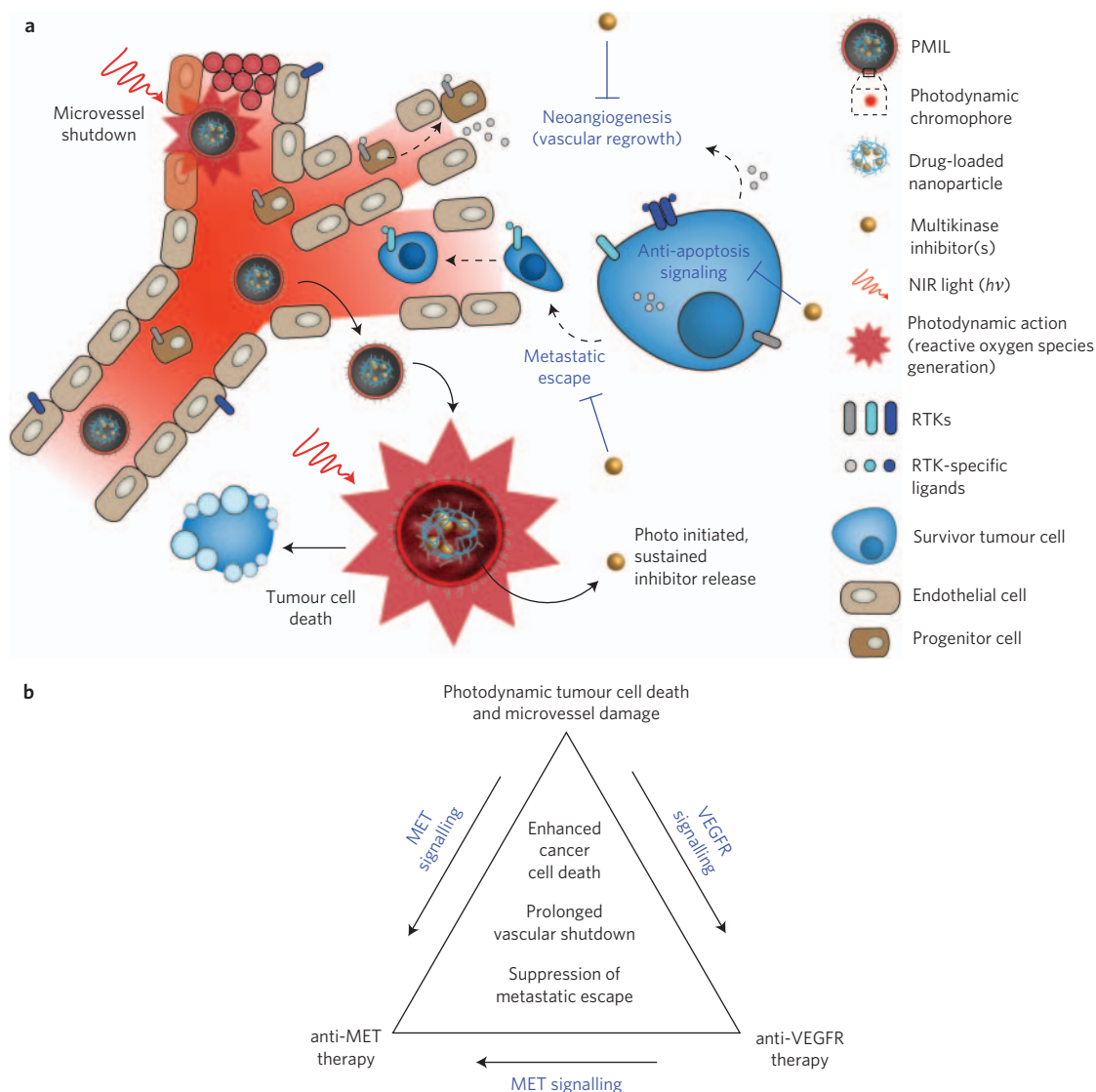
Figure 1 | Concepts of spatiotemporal-synchronized combination therapy using PMILs. a, NIR light activates PMILs within the tumour microvasculature and parenchyma for simultaneous neovascular damage, tumour cell apoptosis and necrosis as well as liposome disruption with initiation of sustained multikinase inhibition. The PMIL delivery system is tuneable for simultaneous delivery of photodynamic, chemotherapeutics and small-molecular inhibitors. **b**, Schematic of a three-way interactive combination therapy with photodynamic tumour cell and microvasculature damage and inhibition of treatment escape pathways. Q2
VEGFR signalling stimulates tumour angiogenesis and preparation of the premetastatic niche via supporting endothelial cell survival, migration and proliferation as well as increased vessel permeability and chemotaxis of bone marrow derived progenitor cells. MET signalling promotes escape from cytotoxic and antiangiogenic therapy via supporting cancer cell survival, motility and metastasis as well as cancer stem-like cell maintenance and tumour angiogenesis via cross talk with the VEGFR pathway. XL184 inhibits activation of both the MET and VEGF signalling pathways to suppress tumour cell survival, metastasis and regrowth following cytotoxic therapy.

tumour growth while mitigating the unwanted consequences of increased intratumoural hypoxia—cancer cell migration and tumour growth along remaining, functional vessels as well as via lymphatic routes[16,17]. Here, we demonstrate that PDAC tumours transiently upregulate MET signalling in response to PDT *in vivo* (Supplementary Fig. 1), which closes the triangle to motivate a three-way interactive therapy (Fig. 1b)—suggesting a compelling rationale to combine concurrent anti-VEGF and -MET therapy with PDT—and motivated development of the PMIL.

This approach—utilizing liposomes loaded with a lipophilic therapeutic agent and encapsulating a PLGA nanoparticle that releases a second, complementary agent—is supported by the reported successes of nanoliposome-based delivery of chemotherapeutics[18,19] (Supplementary Note 1). An advantage of this hybrid drug delivery vehicle is that its lipid[18] and polymer components[20,21] are all in

clinical use and are biodegradable, nontoxic chemicals that can be metabolized by the body. PMILs build on these advances by utilizing light activation not only for photodynamic action but also as a drug release mechanism to enable tumour-focused, spatiotemporally synchronized combination therapies. This opens the door to a number of combination therapies for which capturing and suppressing bursts in molecular signalling dynamics is key.

PMIL design, synthesis and characterization
PMILs were synthesized with the lipophilic photosensitizer BPD formulated within the lipid bilayer of a liposome encapsulating PLGA nanoparticles[20,21] loaded with the hydrophobic multikinase inhibitor XL184 (Fig. 2a–c). The NP[XL184] was engineered to optimize the XL184 loading efficiency (Supplementary Fig. 2) and to be smaller in diameter than the liposomes (Fig. 2d,e) to facilitate

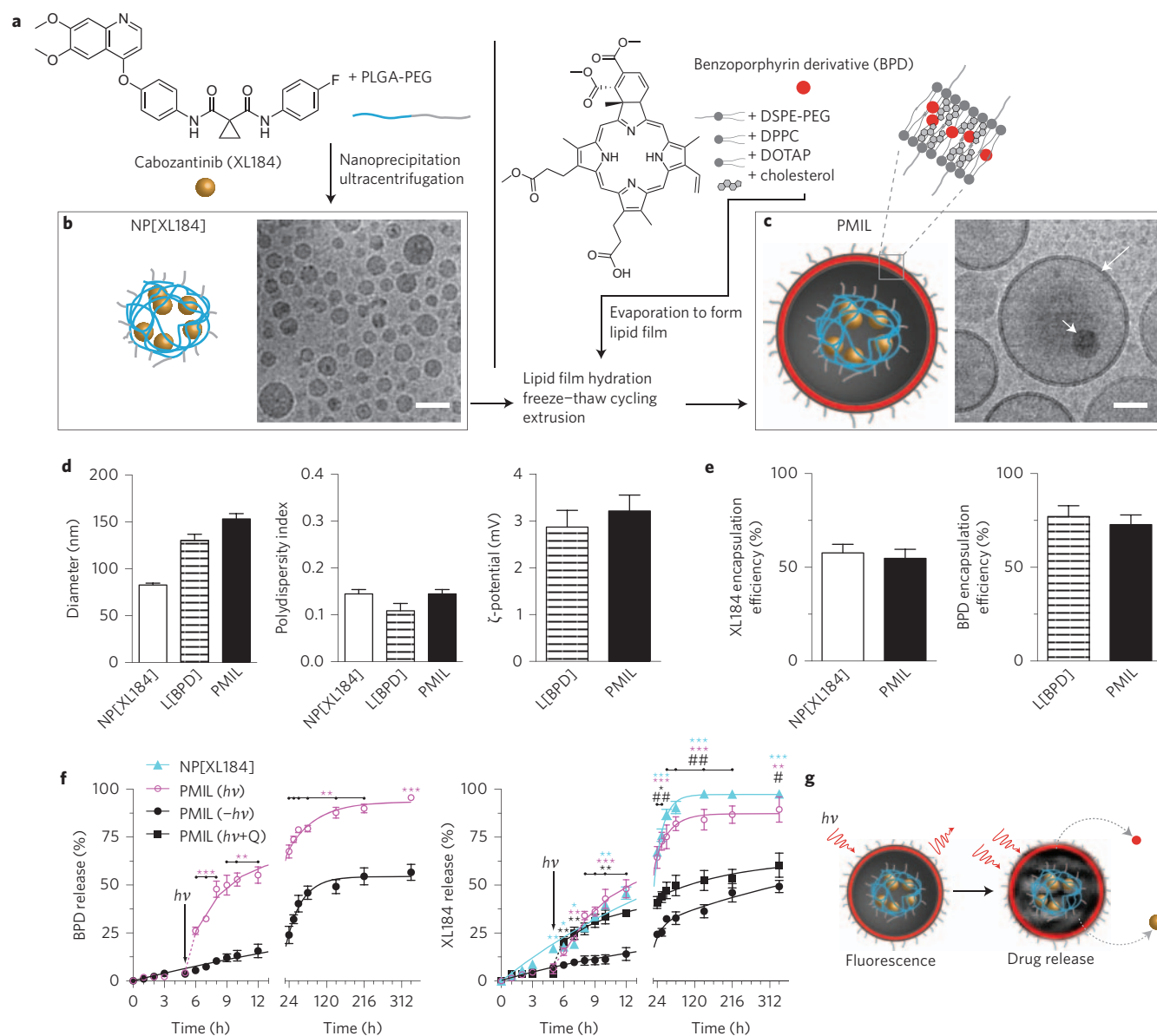**Figure 2 | Synthesis and characterization of a benzoporphyrin–XL184 PMIL. a,** Diagrams of XL184-loaded nanoparticle (NP[XL184]) and BPD-loaded lipid film synthesis. **b,c,** Schematics and representative cryo-electron microscopy (cryo-EM) images of NP[XL184] (**b**) and PMIL (**c**). Arrows and arrowheads indicate the outer lipid bilayer and an encapsulated nanoparticle, respectively, in **c**. Scale bars, 50 nm. **d,e,** Physical characterization of the various nanoconstructs by dynamic light scattering (**d**) and nanoconstruct drug encapsulation efficiencies (**e**). Results are mean ± s.e.m. (NP[XL184] and PMIL, $n = 12$ technical replicates each performed with an independent nanomaterial preparation; L[BPD], $n = 10$ technical replicates each performed with an independent nanomaterial preparation). **f,** Photoinduced drug release from PMILs in serum versus release in the absence of laser irradiation. The arrows indicate that a NIR light dose was given at the 5 h time point (37 °C; 100 mW cm^{-2}; 5 J cm^{-2}). Results are mean ± s.e.m. ($n = 3$ technical replicates each performed with an independent nanomaterial preparation; error is small where not visible). Asterisks and hashes denote significance compared with untreated PMILs (PMIL, −$h\nu$) or NIR-irradiated PMILs (PMIL, $h\nu$) compared with NIR-irradiated PMILs in the presence of sodium azide (a reactive oxygen species scavenger; PMIL, $h\nu$+Q), respectively (*,# $P < 0.05$, **,## $P < 0.01$, *** $P < 0.001$, one-way ANOVA with Tukey's *post hoc* test). Trend lines are fits to a simple one- or two-phase exponential release model (see Methods). **g,** Schematic of PMIL fluorescence imaging and photoinduced drug release. DOTAP, 1,2-dioleoyl-3-trimethylammonium-propane; DPPC, 1,2-dipalmitoly-sn-glycero-3-phosphocholine; DSPE-PEG, 1,2-distearoyl-sn-glycero-3-phosphoethanolamine-N-[methoxy(polyethylene glycol)200]; PLGA-PEG, poly-(lactic acid-co-glycolic) acid–polyethylene glycol conjugate.

its encapsulation within the liposome. In this design, the lipid bilayer acts to protect NP[XL184] from solvent exposure, limiting hydrolysis and systemic XL184 release before photoinduced drug release (Fig. 2f,g and Supplementary Fig. 3). We reasoned that NIR irradiation (using a 690 nm laser matched to BPD absorption) could deposit enough photonic energy to promote BPD-mediated photochemistry at the lipid bilayer and disrupt the integrity of the liposome[4,22] (Supplementary Note 2), thereby exposing the NP

[XL184] to solvents and accelerating the liberation of the payload in the target lesion (Fig. 2f). Reactive oxygen species scavengers significantly suppressed photoinduced XL184 release indicating the involvement of photochemical drug release (Fig. 2f and Supplementary Fig. 4). The 50:50 PLGA ratio used to synthesize the NP[XL184] is designed for sustained XL184 delivery over a period of several days, with an initial burst release on liposome disruption and water contact that is followed by a slower, sustained
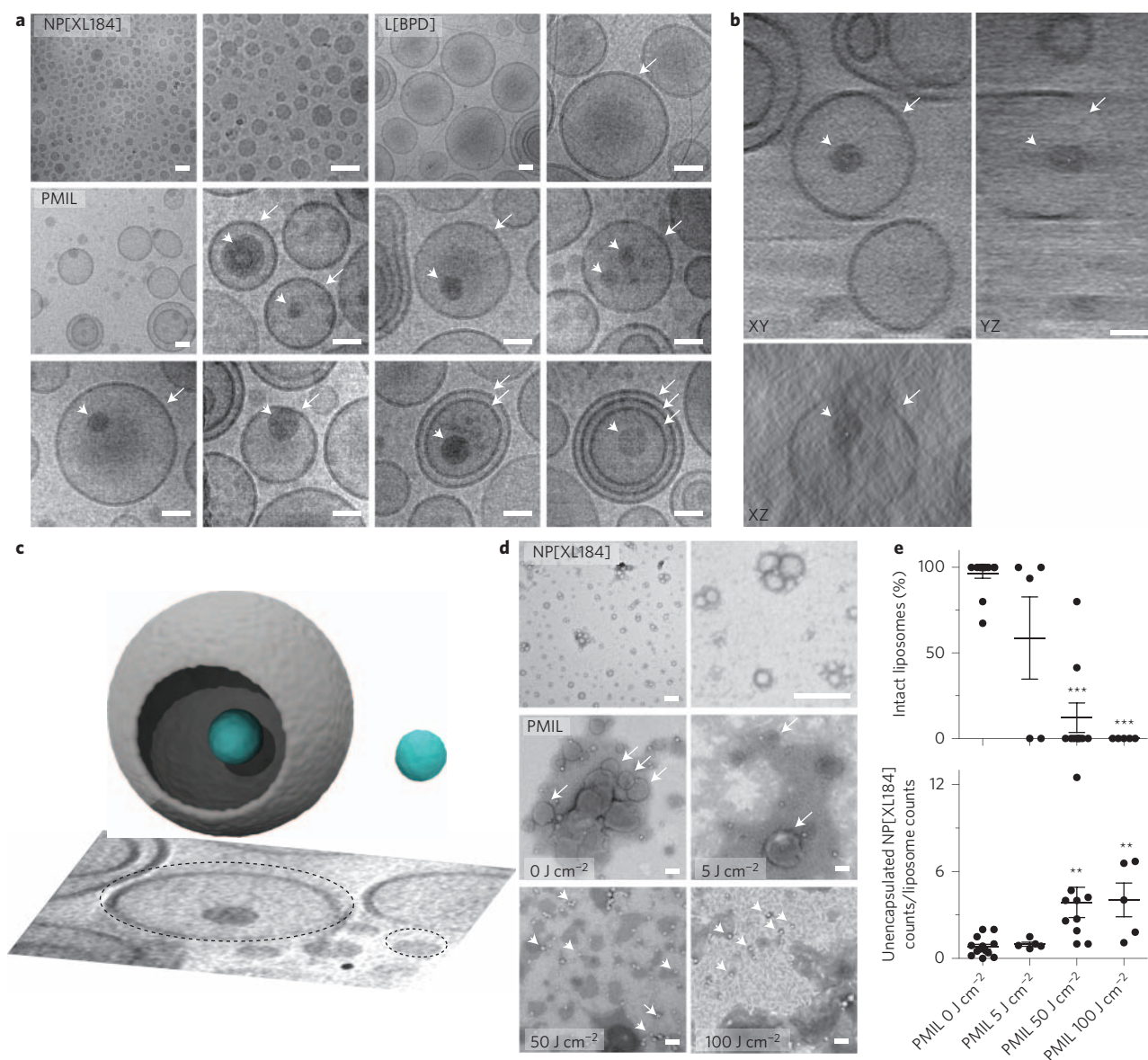
Figure 3 | Structural imaging of NP[XL184] encapsulation and XL184 photorelease from PMILs. a, Representative cryo-EM images of NP[XL184], L[BPD] and PMIL. **b**, Cryo-EM tomogram of a PMIL. Arrows and arrowheads in **a** and **b** indicate the outer lipid bilayer and encapsulated nanoparticles, respectively. Scale bars, 50 nm. Empty liposomes, unencapsulated NP[XL184] and multilamellar liposomes were also observed in the PMIL samples (Supplementary Fig. 5a–c and Supplementary Note 3). **c**, 3D renders of an example PMIL encapsulating a nanoparticle as well as an example of an unencapsulated nanoparticle from a cryo-EM tomogram of a PMIL sample. The dashed circles indicate the rendered objects in the lower 2D tomogram slice. **d**, Representative transmission electron microscopy (TEM) images of NP[XL184] and PMIL treated with varying NIR light doses (100 mW cm^{-2}; 0, 5, 50, or 100 J cm^{-2}), and using negative staining with phosphotungstic acid. Arrows and arrowheads indicate intact liposomes and unencapsulated nanoparticles, respectively. Scale bars, 100 nm. **e**, Quantification of intact liposomes and unencapsulated nanoparticles shown in (**d**) (Supplementary Fig. 5e). Results are mean ± s.e.m. Asterisks in (**e**) denote significance compared with untreated PMILs, 0 J cm^{-2} (PMIL 0 J cm^{-2}, $n = 14$ images; PMIL 5 J cm^{-2}, $n = 5$ images; PMIL 50 J cm^{-2}, $n = 10$ images; PMIL 100 J cm^{-2}, $n = 5$ images; the images were collected from two technical replicates performed with a single nanomaterial preparation for each group; $**P < 0.01$, $***P < 0.001$, Kruskal–Wallis one-way ANOVA).

release phase due to nanoparticle erosion and XL184 diffusion (Fig. 2f)[20]. In contrast, XL184 is released from the PMIL over a period of several weeks in the absence of photoinduced release (Fig. 2f). Electron microscopy indicates a NP[XL184] encapsulation efficiency of ~20% within liposomes (Fig. 3a–c and Supplementary Fig. 5) and disruption of the bilayer following laser irradiation (Fig. 3d,e and Supplementary Fig. 5). Surprisingly, although the majority of NP[XL184] is unencapsulated by a lipid bilayer, light-activated drug release is prominent and might be explained by the self-assembly of lipid monolayers onto PLGA nanoparticles (Supplementary Note 3).

On photorelease, XL184 is liberated to initiate inhibition of multiple kinases (Supplementary Note 4). XL184 is approved by the US Food and Drug Administration for treatment of patients with medullary thyroid cancer, based on a promising phase III trial[23], and is currently in clinical trials for PDAC (NCT01663272) as well as for a number of other malignancies. Because XL184 inhibits escape from anti-VEGF therapy via MET signalling[16] and inhibits pancreatic cancer stem-like cells[14,24], XL184 offers promise for treatment of PDAC in comparison with the poor phase III results for anti-VEGF therapy alone in combination with gemcitabine[25].

In addition to photorelease of NP[XL184], NIR irradiation also triggers BPD-PDT to directly damage microvasculature, cancer cells or both, depending on the time of illumination following BPD administration[26–28]. As an example, BPD-PDT is used routinely in the clinic for selective closure of choroidal neovasculature associated with age-related macular degeneration while sparing the overlying neurosensory retina to preserve visual acuity[29]. For oncological applications, BPD-PDT is often most effective at time points that balance BPD localization in neovasculature with extravasation into the tumour parenchyma (60–90 min post-injection), which induces both microvasculature and cancer cell destruction[26]. In a promising phase I/II clinical trial (VERTPAC), such a BPD-PDT regimen produced a 1–4 cm zone of tumour necrosis with a 100% patient response rate for light delivered via optical fibers positioned percutaneously within locally advanced PDAC tumours under computed tomography guidance[30]. Moreover, the unique mechanisms of cell death induced by PDT[31,32]—including direct damage to Bcl-2 protein (a major anti-apoptotic factor and mediator of drug-resistance) and mitochondrial cytochrome c release (a potent pro-apoptotic signal)—are effective against chemo- and radioresistant cells[33–35] and sensitize cancer cells to chemotherapeutics[33,34] as well as to molecular inhibitors[12,36].

BPD is nontoxic (Supplementary Note 5), however, XL184 possesses significant toxicities that can require concomitant medications, dose interruption or dose reduction[23]. To limit the need for chronic XL184 administration and its systemic exposure to the body, the PMIL was designed to realize tumour-focused release of XL184.

Cellular PMIL internalization and *in vitro* efficacy

Cellular uptake of PMILs and of liposomes loaded with BPD in the bilayer but lacking XL184, L[BPD], was determined by BPD fluorescence confocal microscopy in monolayer cultures of AsPC1 cells derived from metastatic human PDAC ascites (VEGR1+ and MET+ with multiple oncogenic mutations; Supplementary Note 6). Both the PMIL and the L[BPD] underwent cellular internalization (Fig. 4a), with similarity to the pharmaceutical formulation of BPD[35]. BPD-PDT of AsPC1 cells using either L[BPD] or PMILs results in increased MET activation (Fig. 4b,c and Supplementary Fig. 6). PDT-induced MET activation is downregulated using scavengers of reactive oxygen species produced by PDT photochemistry or by inhibiting epidermal growth factor receptor (EGFR)-mediated transactivation of MET (Fig. 4b and Supplementary Note 7). To investigate MET inhibition on PMIL uptake into cancer cells, and photoinduced release of XL184, western blotting was used to measure phosphorylated MET (pMET; activated MET) as well as total MET expression for untreated AsPC1 cells versus cells treated with L[BPD] or PMILs that received a sub-lethal dose of NIR light (1 J cm^{-2}) after a 1 h incubation period (Fig. 4c). BPD-PDT using L[BPD] results in enhanced MET phosphorylation while PMILs suppress MET activation (Fig. 4c). In the absence of photoinduced XL184 release, the PMILs have no effect on the basal pMET level (Fig. 4c). These results indicate that NIR irradiation triggers XL184 release from the PMIL such that the initiation of MET inhibition coincides with photodynamic cytotoxicity. Note that in contrast to photoinduced suppression of MET activation, none of the treatment arms had a significant impact on the total MET level.

Harnessing this photoinduced release of XL184 from PMILs, we hypothesized that simultaneous photocytotoxicity and inhibition of MET activation—and, thereby, suppression of downstream anti-apoptotic survival pathways[14]—could enhance cancer cell death. Note that XL184 also inhibits other receptor tyrosine kinases involved in intra- and autocrine cancer cell signalling, such as VEGFR1 (Supplementary Note 4). Cancer cell death was probed for the following treatments (250 nM BPD and/or 100–125 nM XL184) administered to AsPC1 cells: XL184; NP[XL184]; L[BPD]; co-administration of L[BPD] and NP[XL184] as separate agents; and PMIL. The submicromolar doses of XL184 used here do not induce cancer cell death as a single agent (Fig. 4d and Supplementary Note 8). NIR photoirradiation (690 nm) was performed for a range of light doses (0–10 J cm^{-2}) 1 h post drug administration. L[BPD]- and PMIL-PDT showed a characteristic increase in cell killing with increasing light dose with no dark toxicity. Furthermore, MET inhibition using PMILs induces an enhanced level of cancer cell death in comparison with L[BPD]-PDT as well as in comparison with co-administration of L[BPD] and NP[XL184] as separate agents (Fig. 4d). Collectively, these *in vitro* cancer cell culture studies indicate that inhibition of kinase activation simultaneous with photocytotoxicity can enhance cancer cell death.

PMIL efficacy in two mouse models of pancreatic cancer

The suppression of MET activation and modest enhancement of cancer cell cytotoxicity using the PMIL *in vitro* is promising for *in vivo* application. *In vivo*, the PMIL acts not only on cancer cells but also on paracrine receptor tyrosine kinase signalling, the tumour vasculature, tumour cell motility and metastatic escape, with potential to provide further gains in efficacy compared with conventional drug formulations. For instance, XL184 acts on endothelial cells lining tumour blood[16] and lymphatic[17] vessels (via VEGFR inhibition, for example). To assess the efficacy of PMILs in controlling localized tumours *in vivo*, we performed a single treatment cycle in established xenograft tumours (~50 mm^3 in size) 18 d following subcutaneous implantation of AsPC1 cells in mice. A single intravenous administration of the following treatments was given to the randomized mice: no-treatment control; XL184; NP[XL184]; L[BPD]; co-administration of L[BPD] and NP[XL184] as separate agents; and PMIL. Each formulation contained 0.25 mg kg^{-1} of BPD and/or 0.1–0.125 mg kg^{-1} XL184. Here, NIR irradiation was performed 1 h following injection—via transcutaneous illumination of the tumour—to induce both vascular and cancer cell destruction. In contrast to the continued tumour growth observed for XL184 and BPD-PDT monotherapy, the PMIL-mediated combination therapy exhibited a prolonged reduction in tumour volume over 10 d following a single treatment (Fig. 5a). Compared with the no-treatment control group, the mean tumour reduction following PMIL treatment was 92% (day 37; Fig. 5b). This result contrasts with the monotherapy controls and the combination therapy by conventional co-administration of L[BPD] and NP[XL184] as separate agents—all of which showed marginal anti-tumour effects as a trend in slowing tumour growth but did not achieve a significant reduction in tumour volume (Fig. 5a,b).

To investigate toxicity, metastasis and microvascular effects, and to further probe local tumour control in a another tumour model using PMILs, we next investigated the same treatment arms in a metastatic mouse model by implanting PDAC cells into the pancreas. Mouse weight was monitored before (day 10 post-tumour inoculation) and after (day 24) treatment as a metric of toxicity (Fig. 5c). The gain in mouse weight and 100% survival of the mice through the treatment endpoint (day 24) indicate that PDT combined with low-dose XL184 treatment has low toxicity (Fig. 5c). Furthermore, pancreatic tumour volumes and histopathology (Supplementary Fig. 8) assessed at the treatment endpoint (day 24) corroborate the enhanced local control of the primary tumour, as found in the subcutaneous model for PMILs (Fig. 5d).

These orthotopic pancreatic tumours are hypovascular in comparison with the surrounding pancreatic tissue (Fig. 6a,b). Nevertheless, XL184 ($P = 0.19$, Mann-Whitney U test) and PMIL-treatment ($P = 0.20$, Mann-Whitney U test) selectively induced trends in reduced intratumoural—but not peritumoural—microvessel

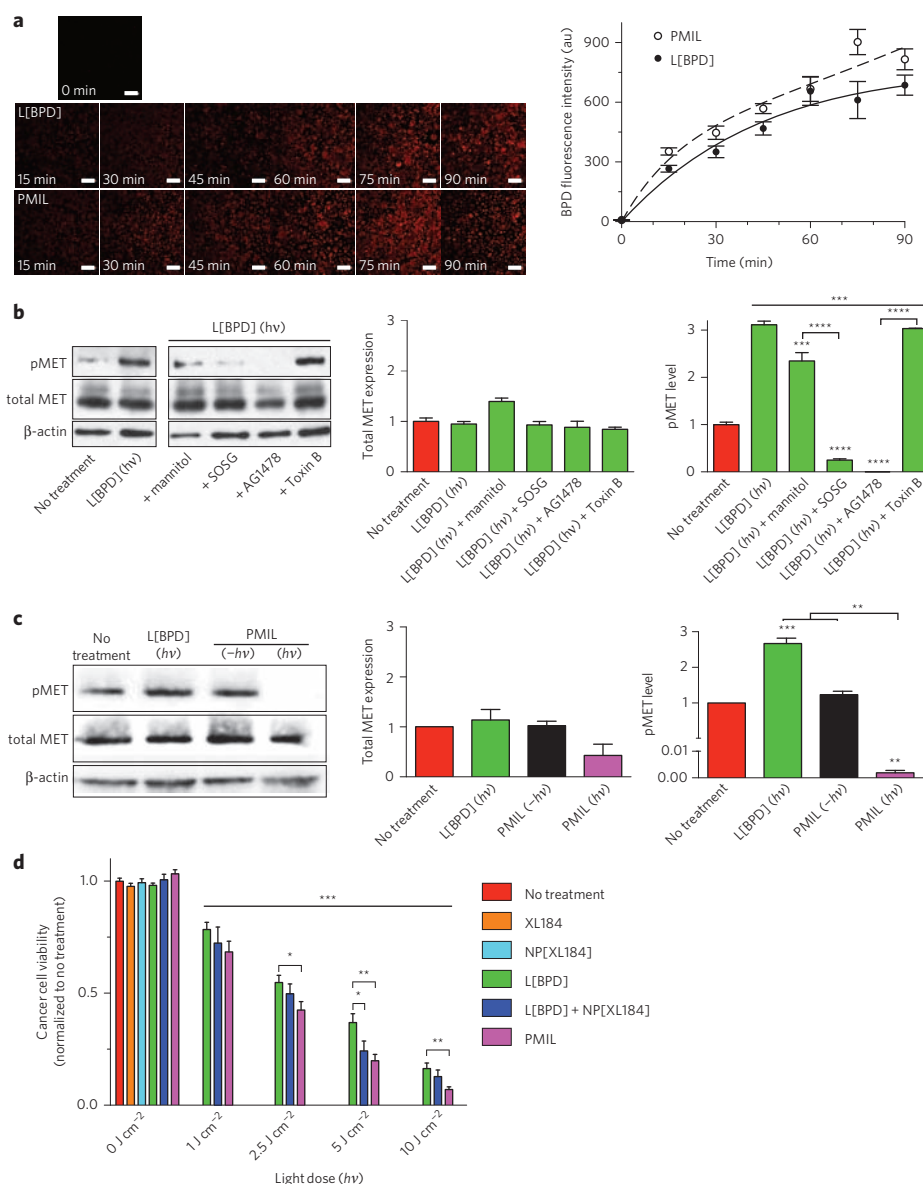**Figure 4 | MET inhibition enhancement of PDT-induced cancer cell death *in vitro* using PMILs. a**, Representative confocal BPD fluorescence (red) microscopy images and quantification of BPD fluorescence during L[BPD] and PMIL cellular uptake in monolayer AsPC1 cell cultures (no light irradiation for therapy). The image at 0 min represents the minimal live cell autofluorescence before adding L[BPD] or PMIL, and later time points demonstrate increasing cellular accumulation of BPD resulting from nanoconstruct internalization. Results are mean ± s.e.m. (*n* = 3 biological replicates per condition × 3 images per replicate). Trend lines are fits to a simple pharmacokinetic model (Methods). **b**, Western blotting and quantification of total MET and pMET expression—normalized to β-actin and relative to the no-treatment control group (normalized to 1)—indicate that pMET increases 24 h following PDT with L[BPD] (L[BPD]-PDT; 125 nM BPD; 690 nm; 100 mW cm^{-2}; 2.5 J cm^{-2}), whereas there is no significant change in overall MET protein expression following PDT over a range of PDT doses (Supplementary Fig. 6). A singlet oxygen-specific scavenger (Singlet Oxygen Sensor Green, SOSG; 100 μM) inhibits L[BPD]-PDT activation of MET signalling, whereas a free radical scavenger (mannitol, 50 mM) has only a modest affect. In addition, an EGFR-specific kinase inhibitor, AG1478 (12.5 nM), also inhibits MET activation following PDT whereas toxin B (2 ng ml^{-1}), an inhibitor of GPCR-mediated MET transactivation, has no effect. Results are mean ± s.e.m. Underlined asterisks denote significance compared with no treatment, and the remaining asterisks denote significance compared with L[BPD]-PDT, L[BPD] (*hv*), or amongst the indicated groups (*n* = 3 biological replicates per condition; ***P < 0.001, ****P < 0.0001, one-way ANOVA with Tukey's *post hoc* test). **c**, Western blots and quantification of photoinduced suppression of MET activation (pMET) using PMILs 24 h following treatment. In contrast to increased pMET following L[BPD]-PDT, MET activation is suppressed following PDT with PMILs (250 nM BPD; 690 nm; 100 mW cm^{-2}; 1 J cm^{-2}). Without photoinduced XL184 release (PMIL, −*hv*), the PMIL has no effect on the basal levels of pMET. Results are mean ± s.e.m. (*n* = 2 biological replicates per condition; **P < 0.01, ***P < 0.001, one-way ANOVA with Tukey's *post hoc* test). **d**, MTT assay of AsPC1 cell viability following XL184 and PDT monotherapy or combination therapy. Results are mean ± s.e.m. Asterisks denote significance compared with no treatment or amongst the indicated groups (No-treatment control and L[BPD] 0 J cm^{-2}, *n* = 17 biological replicates; XL184, *n* = 10 biological replicates; NP[XL184], *n* = 16 biological replicates; L[BPD] + NP[XL184] 0 and 1 J cm^{-2}, *n* = 5 biological replicates; L[BPD] 1 J cm^{-2}, L[BPD] + NP[XL184] 2.5, 5 and 10 J cm^{-2}, PMIL 0 and 1 J cm^{-2}, *n* = 8 biological replicates; L[BPD] 2.5, 5 and 10 J cm^{-2}, and PMIL 2.5, 5 and 10 J cm^{-2}, *n* = 11 biological replicates; *P < 0.05, **P < 0.01, ***P < 0.001, one-way ANOVA with Tukey's *post hoc* test). Fisher's least significant difference *post hoc* test of the integrated PDT dose response curves (analysis of the area under the curve mean and standard error) indicates that the PMIL achieves enhanced cancer cell death versus L[BPD] + NP[XL184] (*P* < 0.05) and L[BPD] (*P* < 0.001) (Supplementary Fig. 7a).
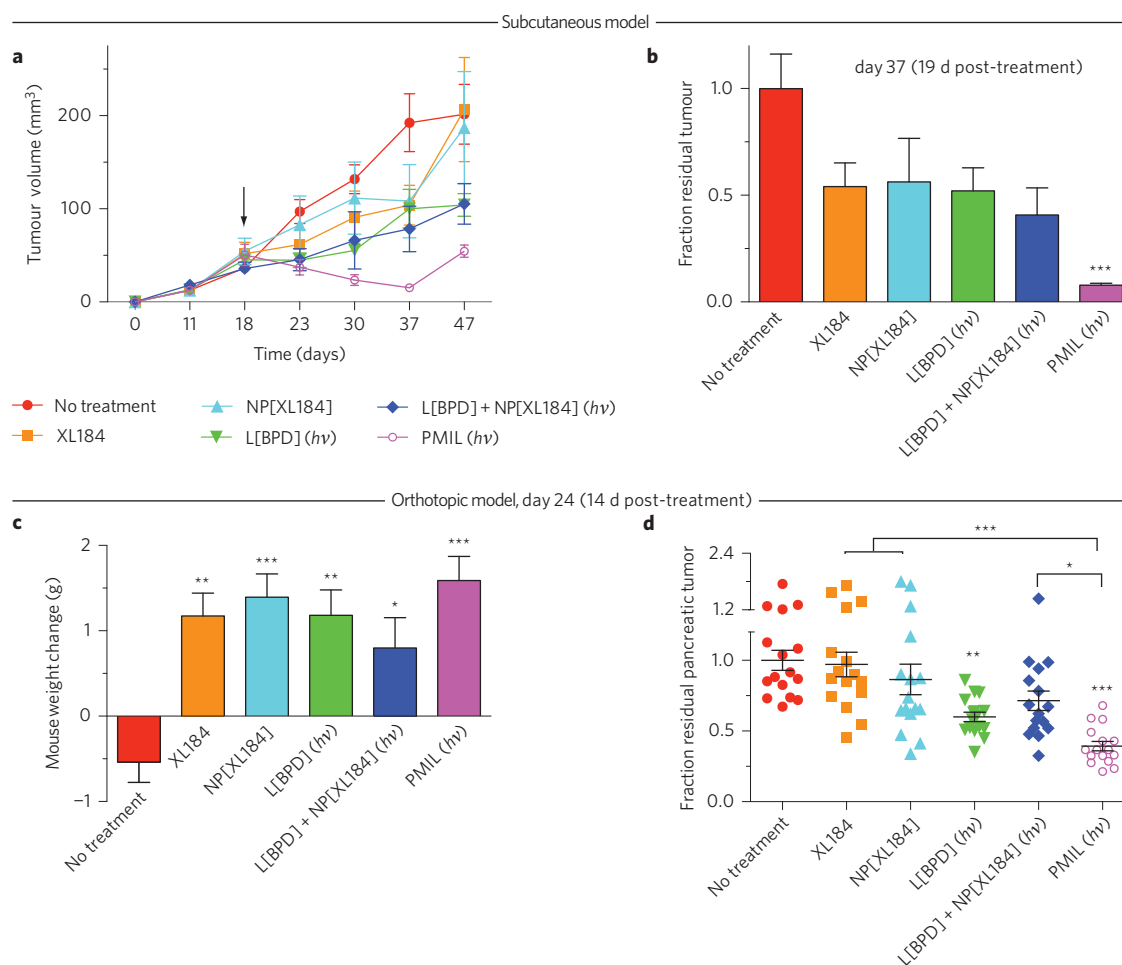
Figure 5 | Prolonged tumour reduction *in vivo* with a single cycle of PMIL-treatment. a,b, Combined BPD-PDT (690 nm; 100 mW cm^{-2}; 75 J cm^{-2}) and XL184 treatment using PMILs achieves prolonged reductions in subcutaneous tumour volumes (**a**) with a minimal fractional residual tumour on day 37 (**b**). The arrow in **a** indicates administration of a single treatment cycle. Results are mean ± s.e.m. Error is small where hidden. Asterisks in **b** denote significance compared with no treatment ($n = 5$ mice per group; ***$P = 0.0038$, Kruskal–Wallis one-way ANOVA). **c,d**, Orthotopic PDAC mouse weight change (**c**; compared with 10 d post-tumour inoculation, before treatment) and pancreatic tumour volume (**d**) at the experiment endpoint (37 d following tumour inoculation). Results are mean ± s.e.m. Asterisks denote significance compared with no treatment or amongst the indicated groups ($n = 16$ mice per group; *$P < 0.05$, **$P < 0.01$, ***$P < 0.001$, Kruskal–Wallis one-way ANOVA). A single cycle of combination therapy using PMILs achieves enhanced reductions in orthotopic tumours ($P = 0.011$, two-way ANOVA BPD-PDT·XL184 interaction term; Supplementary Fig. 7b and Supplementary Tables 1 and 2)—but not using the conventional combination, L[BPD] + NP[XL184] ($P = 0.23$).

density versus the no-treatment control tumours (Fig. 6b). Because of the substantial degree of tumour shrinkage by PMILs (Fig. 5d), which tends to compact the remaining vasculature and to obscure interpretation of microvessel density[37], we also estimated the intra-tumoural microvessel volume using an immunofluorescence and digital slide scanning microscopy technique to efficiently sample the endothelial cell content of entire tumour volumes[38] (see Methods and Supplementary Note 9). The intratumoural microves-sel volume estimate revealed a significant reduction in total tumour microvascularity achieved by the PMIL, which suggests an antivas-cular effect facilitated by PDT with suppression of vascular and tumour regrowth by sustained XL184 release. Furthermore, invasive tumour borders and metastatic infiltrates within the surrounding pancreatic tissue characterize this orthotopic model of PDAC (Fig. 6a). Metastases in the liver and retroperitoneal lymph nodes appear rapidly in this model, as assessed by a quantitative polymer-ase chain reaction assay (Methods) that measures the number of viable human metastatic cancer cells in organ biopsies (Fig. 6d). The single PMIL treatment achieved a 98.7% mean reduction in liver and retroperitoneal lymph node metastasis compared with

the no-treatment control group at the treatment endpoint (day 24), while the other treatment groups did not achieve a statistically significant change in metastasis (Fig. 6d).

The local tumour reduction and suppression of metastasis result-ing from a single PMIL treatment contrasts with the use of XL184 as a single agent, which is given daily over an extended period by oral administration. For instance, 99% primary tumour reduction, 79% microvessel density reduction and 100% liver metastasis reduction were reported in a mouse model of pancreatic neuroendocrine tumours (40 mg kg^{-1} XL184, administered daily for 3 weeks)[16]. Here, a single PMIL treatment (including 0.1–0.125 mg kg^{-1} XL184) achieved 92 and 61% reductions of subcutaneous and orthotopic PDAC tumours, respectively, with 70% intratumoural microvessel volume reduction and 99% metastatic cancer cell reduction in the liver and regional lymph nodes. Remarkably, the interaction of PDT with photoinitiated and sustained XL184 release facilitated by the PMIL enables the same therapeutic efficacy of daily oral XL184 monotherapy with less than a thousandth (~1/6,700) of the XL184 dosage (Supplementary Note 10). This indicates that the PMILs offer a significant potential to reduce
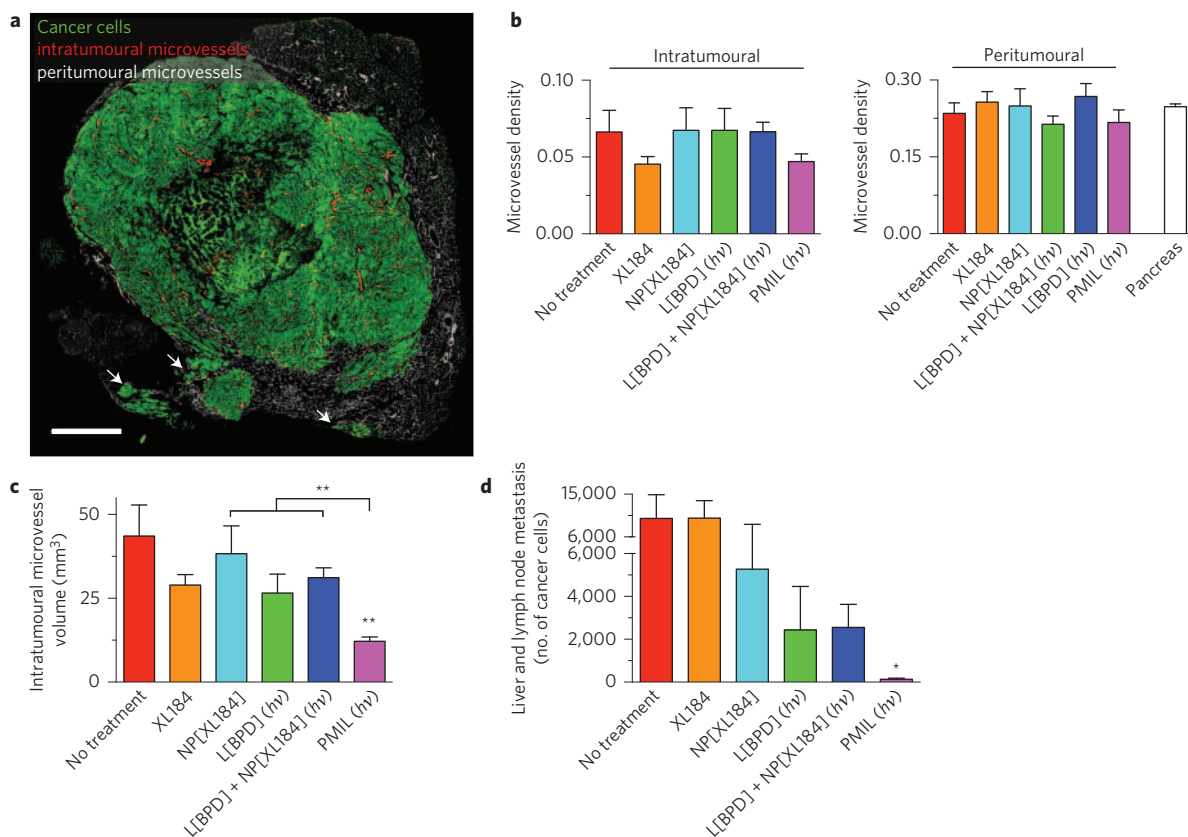
Figure 6 | Antivascular and antimetastatic effects using a single PMIL-treatment cycle *in vivo*. a, A representative confocal fluorescence image mosaic of an entire orthotopic PDAC tumour cross-section with 1.2 μm x–y sampling illustrates selective immunostaining of human epithelial cancer cells (green) to discriminate intra- (red) and peritumoural (gray scale) endothelial cells. Arrows indicate local metastases and cancer cells infiltrating the surrounding pancreatic tissue. Scale bar, 1 mm. **b**, Intra- and peritumoural microvessel densities at the treatment endpoint. **c**, A single PMIL treatment induces a decrease in intratumoural microvessel volume. Results are mean ± s.e.m. Asterisks denote significance compared with no treatment or amongst the indicated groups (no-treatment control, *n* = 8 entire tumour cross-section image mosaics from 8 mice; XL184, *n* = 7 entire cross-sections from 3 mice; NP[XL184], *n* = 8 entire cross-sections from 4 mice; L[BPD], 8 entire cross-sections from 4 mice; L[BPD] + NP[XL184], 10 entire cross-sections from 5 mice; PMIL, 10 entire cross-sections from 7 mice; **P* < 0.01, Kruskal–Wallis one-way ANOVA). **d**, A single PMIL treatment reduces the number of total number of metastatic cancer cells in the liver and regional lymph nodes. Results are mean ± s.e.m. Asterisks denote significance compared with no treatment (no-treatment control, NP[XL184], L[BPD] + NP[XL184], and PMIL, *n* = 20 mice per group; XL184, *n* = 18 mice; L[BPD], *n* = 16 mice; **P* < 0.05, Kruskal–Wallis one-way ANOVA).

systemic exposure to XL184, reducing the risks of toxic side effects and the need for dose interruptions.

The *in vivo* efficacy of PMIL also contrasts strongly with co-administration of L[BPD] and NP[XL184] as separate agents. The PMIL unites the pharmacokinetics of L[BPD] and NP[XL184] delivery and enables tumour-confined, photoinduced XL184 release, while the conventional delivery of L[BPD] and NP[XL184] precludes a full interaction between these therapies. The enhanced efficacy of the PMIL highlights the importance of co-packaging interactive therapeutic agents into one carrier with spatiotemporally synchronized release. Note that although XL184 had no cytotoxicity as a single agent *in vitro* (Fig. 4d), PMIL treatment achieved super-additive cancer cell killing both *in vitro* and *in vivo* (Supplementary Fig. 7), which suggests a synergistic interaction between XL184 and BPD-PDT facilitated by the PMIL (Supplementary Note 11). The requirement for co-packaging to achieve maximal impact is probably due to rapid (within 1–4 h) microvessel damage and shutdown by both XL184[39] and BPD[27] that mutually compromise co-delivery of these therapies as separate agents using conventional drug delivery formulations. The rapid vascular effects of PDT in particular (<1 h for blood flow stasis onset with a duration > 48 h[27]) would preclude XL184 delivery during the critical time window for anti-apoptotic signalling and vascular regrowth inhibition during the burst in tumour VEGF (within 6 h[40]) and MET (within 72 h; Supplementary Fig. 1) signalling that follows cytotoxic therapy. Rapid PDT-induced vascular shutdown would inhibit overall XL184 delivery (55 h half-life) whereas nanoparticles entrapped in the tumour release XL184 locally for a sustained period to inhibit vascular regrowth and metastasis following PDT. XL184 could be administered before PDT but this still precludes sustained therapeutic doses of XL184 until tumour vascular regrowth following PDT.

Conclusions

In summary, the complexities of cancer necessitate the innovation of drug delivery platforms that are capable of addressing multiple tumour compartments as well as treatment escape mechanisms. An emerging paradigm in cancer therapy suggests that gains in local tumour control can be compromised by co-activation of multiple tumour survival signalling pathways that promote increased invasiveness and metastasis[5,8]. This aggressive response to treatment may ultimately limit patient survival. Combination therapies hold great promise for overcoming this paradox by addressing the mechanisms of tumour recurrence and treatment escape. However, co-activation of multiple tumour survival signalling pathways and microvessel shutdown limit the efficacy of sequential drug delivery. New drug delivery systems are needed to facilitate combinations that span cytotoxic, antivascular and anti-invasive mechanisms. To

address these challenges, we developed PMILs that integrate the antivascular and antiangiogenic mechanisms of photodynamic and anti-VEGF therapy while blocking tumour cell invasion, metastasis and escape via the MET pathway. This approach is inspired by recent advances in photoactivated nanomaterials[2,4], multi-drug loaded[41] as well as stimuli-responsive liposomes[42] and by the nano-cell platform[43], which introduced extrinsically activated drug release, maintenance of synergistic drug ratios and temporal targeting of distinct tumour compartments, respectively. PMILs utilize these features for multi-agent co-delivery with photorelease and entrapment of NP[XL184] within the tumour following vascular shutdown for sustained release. This approach uniquely enables a tumour-confined, spatiotemporally synchronized multi-modal combination therapy at the 'right time and right place'. The PMIL attenuates metastatic outgrowth and escape but the photodynamic component is limited at present to localized tumours and further developments will be needed to address established distal metastases. Note that XL184 is eventually released from the PMIL in the dark (Fig. 2f) such that established metastases will be impacted by passive tumour accumulation of PMILs via the enhanced permeability and retention effect.

Future work will address models of advanced metastatic disease and will potentially involve further developments to incorporate targeted and activable delivery for wide-field PDT with sufficient selectivity to treat disseminated micrometastases[44]. The role of the unencapsulated NP[XL184] population, and the possibility of a BPD-loaded lipid monolayer that contributes to light-activated therapy, will also be the subject of future studies. Alternatively, it is possible that the encapsulated NP[XL184] is the dominant contributor such that further reduction in the XL184 dose and systemic toxicity may be achieved by purification of the encapsulated NP[XL184]. Collectively, the present study demonstrates that PMILs maximize therapeutic efficacy per treatment cycle and further studies are warranted to investigate the long-term impacts on cure rate, survival and potentiation of standard chemotherapy regimens. The continuing phase II/III studies of PDT in PDAC form a good basis for developing this approach further.

Methods

Methods and any associated references are available in the online version of the paper.

References

1. Cheng, Z., Al Zaki, A., Hui, J. Z., Muzykantov, V. R. & Tsourkas, A. Multifunctional nanoparticles: cost versus benefit of adding targeting and imaging capabilities. *Science* **338,** 903–910 (2012).
2. Lovell, J. F. *et al.* Porphysome nanovesicles generated by porphyrin bilayers for use as multimodal biophotonic contrast agents. *Nature Mater.* **10,** 324–332 (2011).
3. Cui, S. *et al.* In vivo targeted deep-tissue photodynamic therapy based on near-infrared light triggered upconversion nanoconstruct. *ACS Nano* **7,** 676–688 (2013).
4. Carter, K. A. *et al.* Porphyrin-phospholipid liposomes permeabilized by near-infrared light. *Nature Commun.* **5,** 3546 (2014).
5. Sennino, B. & McDonald, D. M. Controlling escape from angiogenesis inhibitors. *Nat. Rev. Cancer* **12,** 699–709 (2012).
6. Holohan, C., Van Schaeybroeck, S., Longley, D. B. & Johnston, P. G. Cancer drug resistance: an evolving paradigm. *Nat. Rev. Cancer* **13,** 714–726 (2013).
7. Pennacchietti, S. *et al.* Hypoxia promotes invasive growth by transcriptional activation of the met protooncogene. *Cancer Cell* **3,** 347–361 (2003).
8. Pàez-Ribes, M. *et al.* Antiangiogenic therapy elicits malignant progression of tumors to increased local invasion and distant metastasis. *Cancer Cell* **15,** 220–231 (2009).
9. Gorski, D. H. *et al.* Blockade of the vascular endothelial growth factor stress response increases the antitumor effects of ionizing radiation. *Cancer Res.* **59,** 3374–3378 (1999).
10. Tran, J. *et al.* A role for survivin in chemoresistance of endothelial cells mediated by VEGF. *Proc. Natl Acad. Sci. USA* **99,** 4349–4354 (2002).
11. Justinger, C. *et al.* Increased growth factor expression after hepatic and pancreatic resection. *Oncol. Rep.* **20,** 1527–1531 (2008).
12. Ferrario, A. *et al.* Antiangiogenic treatment enhances photodynamic therapy responsiveness in a mouse mammary carcinoma. *Cancer Res.* **60,** 4066–4069 (2000).
13. Solban, N. *et al.* Mechanistic investigation and implications of photodynamic therapy induction of vascular endothelial growth factor in prostate cancer. *Cancer Res.* **66,** 5633–5640 (2006).
14. Hage, C. *et al.* The novel c-Met inhibitor cabozantinib overcomes gemcitabine resistance and stem cell signaling in pancreatic cancer. *Cell Death Dis.* **4,** e627 (2013).
15. Gherardi, E., Birchmeier, W., Birchmeier, C. & Vande Woude, G. Targeting MET in cancer: rationale and progress. *Nat. Rev. Cancer* **12,** 89–103 (2012).
16. Sennino, B. *et al.* Suppression of tumor invasion and metastasis by concurrent inhibition of c-Met and VEGF signaling in pancreatic neuroendocrine tumors. *Cancer Discov.* **2,** 270–287 (2012).
17. Sennino, B., Ishiguro-Oonuma, T., Schriver, B. J., Christensen, J. G. & McDonald, D. M. Inhibition of c-Met reduces lymphatic metastasis in RIP-Tag2 transgenic mice. *Cancer Res.* **73,** 3692–3703 (2013).
18. Drummond, D. C., Meyer, O., Hong, K., Kirpotin, D. B. & Papahadjopoulos, D. Optimizing liposomes for delivery of chemotherapeutic agents to solid tumors. *Pharmacol. Rev.* **51,** 691–743 (1999).
19. Davis, M. E., Chen, Z. G. & Shin, D. M. Nanoparticle therapeutics: an emerging treatment modality for cancer. *Nat. Rev. Drug Discov.* **7,** 771–782 (2008).
20. Makadia, H. K. & Siegel, S. J. Poly lactic-co-glycolic acid (PLGA) as biodegradable controlled drug delivery carrier. *Polymers* **3,** 1377–1397 (2011).
21. Hines, D. J. & Kaplan, D. L. Poly(lactic-co-glycolic) acid-controlled-release systems: experimental and modeling insights. *Crit. Rev. Ther. Drug Carrier Syst.* **30,** 257–276 (2013).
22. Thompson, D. H., Gerasimov, O. V., Wheeler, J. J., Rui, Y. & Anderson, V. C. Triggerable plasmalogen liposomes: improvement of system efficiency. *Biochim. Biophys. Acta* **1279,** 25–34 (1996).
23. Elisei, R. *et al.* Cabozantinib in progressive medullary thyroid cancer. *J. Clin. Oncol.* **31,** 3639–3646 (2013).
24. Li, C. *et al.* c-Met is a marker of pancreatic cancer stem cells and therapeutic target. *Gastroenterology* **141,** 2218–2227.e5 (2011).
25. Kindler, H. L. *et al.* Gemcitabine plus bevacizumab compared with gemcitabine plus placebo in patients with advanced pancreatic cancer: phase III trial of the Cancer and Leukemia Group B (CALGB 80303). *J. Clin. Oncol.* **28,** 3617–3622 (2010).
26. Chen, B., Pogue, B. W., Hoopes, P. J. & Hasan, T. Combining vascular and cellular targeting regimens enhances the efficacy of photodynamic therapy. *Int. J. Radiat. Oncol. Biol. Phys.* **61,** 1216–1226 (2005).
27. Fingar, V. H. *et al.* Analysis of acute vascular damage after photodynamic therapy using benzoporphyrin derivative (BPD). *Br. J. Cancer* **79,** 1702–1708 (1999).
28. Kurohane, K. *et al.* Photodynamic therapy targeted to tumor-induced angiogenic vessels. *Cancer Lett.* **167,** 49–56 (2001).
29. Schmidt-Erfurth, U. & Hasan, T. Mechanisms of action of photodynamic therapy with verteporfin for the treatment of age-related macular degeneration. *Surv. Ophthalmol.* **45,** 195–214 (2000).
30. Huggett, M. T. *et al.* Phase I/II study of verteporfin photodynamic therapy in locally advanced pancreatic cancer. *Br. J. Cancer* **110,** 1698–1704 (2014).
31. Kessel, D. & Luo, Y. Photodynamic therapy: A mitochondrial inducer of apoptosis. *Cell. Death Diffe.r* **6,** 28–35 (1999).
32. Kessel, D. Death pathways associated with photodynamic therapy. *Med. Laser Appl.* **21,** 219–224 (2006).
33. Duska, L. R., Hamblin, M. R., Miller, J. L. & Hasan, T. Combination photoimmunotherapy and cisplatin: effects on human ovarian cancer ex vivo. *J. Natl Cancer Inst.* **91,** 1557–1563 (1999).
34. Rizvi, I. *et al.* Synergistic enhancement of carboplatin efficacy with photodynamic therapy in a three-dimensional model for micrometastatic ovarian cancer. *Cancer Res.* **70,** 9319–9328 (2010).
35. Celli, J. P., Solban, N., Liang, A., Pereira, S. P. & Hasan, T. Verteporfin-based photodynamic therapy overcomes gemcitabine insensitivity in a panel of pancreatic cancer cell lines. *Lasers Surg. Med.* **43,** 565–574 (2011).
36. del Carmen, M. G. *et al.* Synergism of epidermal growth factor receptor-targeted immunotherapy with photodynamic treatment of ovarian cancer in vivo. *J. Natl Cancer Inst.* **97,** 1516–1524 (2005).
37. Hlatky, L., Hahnfeldt, P. & Folkman, J. Clinical application of antiangiogenic therapy: microvessel density, what it does and doesn't tell us. *J. Natl Cancer Inst.* **94,** 883–893 (2002).
38. Spring, B. Q. *et al.* Efficient measurement of total tumor microvascularity ex vivo using a mathematical model to optimize volume subsampling. *J. Biomed. Opt.* **18,** 096015 (2013).

39. Yakes, F. M. *et al*. Cabozantinib (XL184), a novel MET and VEGFR2 inhibitor, simultaneously suppresses metastasis, angiogenesis, and tumor growth. *Mol. Cancer Ther.* **10,** 2298–2308 (2011).

40. Chang, S. K., Rizvi, I. & Solban, N. In vivo optical molecular imaging of vascular endothelial growth factor for monitoring cancer treatment. *Clin. Cancer Res.* **14,** 4146–4153 (2008).

41. Tardi, P. *et al*. In vivo maintenance of synergistic cytarabine:daunorubicin ratios greatly enhances therapeutic efficacy. *Leuk. Res.* **33,** 129–139 (2009).

42. Dromi, S. *et al*. Pulsed-high intensity focused ultrasound and low temperature-sensitive liposomes for enhanced targeted drug delivery and antitumor effect. *Clin. Cancer Res.* **13,** 2722–2727 (2007).

43. Sengupta, S. *et al*. Temporal targeting of tumour cells and neovasculature with a nanoscale delivery system. *Nature* **436,** 568–572 (2005).

44. Spring, B. Q. *et al*. Selective treatment and monitoring of disseminated cancer micrometastases in vivo using dual-function, activatable immunoconjugates. *Proc. Natl Acad. Sci. USA* **111,** E933–E942 (2014).

Acknowledgements

Author contributions

B.Q.S., R.B.S., L.Z.Z., and T.H. conceived and designed experiments. B.Q.S., R.B.S., L.Z.Z., Z.M., R.W., M.E.S., and E.V. performed experiments. R.B.S. synthesized the nanomaterials. B.Q.S., R.B.S. and E.V. developed methodology and performed data analysis. D.A.S. contributed to statistical analysis of the data. B.Q.S., R.B.S., L.Z.Z., and T.H. prepared the manuscript. B.W.P., S.P.P. and E.V. contributed to experimental design and manuscript preparation. All authors contributed to editing the final manuscript.

Additional information

Competing financial interests

Q7

Methods

NP[XL184] synthesis and characterization. Before NP[XL184] synthesis, the biodegradable copolymer PLGA 50:50 (17 kDa; 0.18 dL g^{-1}; Lake Shore Biomaterials) was modified to incorporate a PEG moiety (COOH-PEG-NH$_2$; 3.5 kDa; JenKem Technology), which enhances both nanoparticle stability and circulation time[18]. Synthesis was then performed by nanoprecipitation[45]. To achieve maximal XL184 loading, nanoparticles were synthesized with various XL184 (>99.0% purity; Selleck Chemicals) and PEG-PLGA drug/polymer ratios ranging from 1–10% (w/w). Of the tested ratios, the XL184 molar loading efficiency was maximal at a drug/polymer (w/w) ratio of 1% (Supplementary Fig. 2). In addition, a range of solvent:water ratios (1:2–1:10) were tested and the optimal ratio for NP[XL184] formation was 1:3 acetone:water. For the optimized synthesis protocol, XL184 was co-solubilized in 1 ml of acetone with PLGA-PEG at a 1% (w/w) drug to polymer concentration. Nanoprecipitation was achieved by adding this mixture dropwise using a 27.5-gauge needle to 3 ml of H$_2$O stirred magnetically at 400 rpm. The reaction mixture was then stirred uncovered for 6 h to allow acetone evaporation, passed through a 0.2 µm filter and purified by ultrafiltration (Amicon-Millipore; 30 kDa cut-off) at 2,500 rpm for 10 min with intermittent washing (4 cycles; 4 ml phosphate-buffered saline per wash). The XL184–PLGA nanoparticle loading efficiency was determined by optical absorption measurements following solvation of the nanoparticles in dimethyl sulfoxide, using the formula: 100·(no. of moles following purification/no. of moles available for synthesis). All NP[XL184] size and charge measurements were made by dynamic light scattering (Malvern, Zetasizer Nano ZS).

PMIL synthesis and characterization. PMILs co-encapsulating BPD (verteporfin; VWR International) and NP[XL184] were prepared by modification of existing synthesis methods[43]. The lipids (DPPC, DOTAP, cholesterol, and DSPE-PEG; Avanti Polar Lipids) were each dissolved separately in chloroform, and then mixed together in a molar ratio of 2:0.2:1:0.2 (DPPC:DOTAP:cholesterol:DSPE-PEG) with 100 nmoles of BPD. This lipid composition was selected on the basis of the previously reported pharmacological success of similar compositions[18]. Inclusion of the cationic lipid, DOTAP, resulted in a zeta potential (surface charge) of +3 mV. This slightly cationic surface charge promotes cellular uptake without significant cytotoxicity to maintain biocompatibility[46]. To form thin lipid films containing BPD, chloroform was removed by rotoevaporation and by placing the sample under vacuum overnight. Next, lipid film hydration was achieved by adding NP[XL184] (50 nmoles of XL184) in 1 ml of phosphate-buffered saline. To ensure adequate encapsulation of NP[XL184], the thin film was subjected to 10 freeze-thaw cycles (6 min per cycle) at 0 and 45 °C, below and above the highest transition temperature of the lipid mixture (DPPC; T_m = 41 °C). The resulting dispersion of multilamellar liposomes was extruded through a 200 nm diameter polycarbonate membrane using a mini-extruder system (Avanti Polar Lipids) to form unilamellar liposomes. BPD and XL184 not loaded into the PMIL were removed by dialysis (Spectra/Por; 300 kDa cutoff; 1 ml sample in 4 l of phosphate-buffered saline at 4 °C for 18 h). During the dialysis period, the sample was analysed by dynamic light scattering measurements. Initially, these measurements indicated a bimodal distribution with peaks at 80 nm (NP[XL184]) and 150 nm (PMIL), which gradually became a single monodispersive peak (PDI < 0.2) as purification of the PMILs completed. However, electron microscopy revealed the presence of residual NP[XL184] not incorporated within liposomes within the PMIL samples (Supplementary Note 3). The PMIL BPD and XL184 concentrations and loading efficiencies were determined by fluorescence and absorbance spectroscopy or by high-performance liquid chromatography (Hydrosil C18 ODS; 2.0 × 14.0 cm; 50% acetonitrile in H$_2$O → 100% acetonitrile; 0.5 h), respectively, following solvation of the PMILs in dimethyl sulphoxide. All PMIL size and charge measurements were made by dynamic light scattering (Malvern, Zetasizer Nano ZS). L[BPD] was synthesized analogously to the PMIL, but without NP[XL184].

PMIL stability and drug photorelease kinetics. PMIL and NP[XL184] size stability during storage at 4 °C was investigated by repeated dynamic light scattering measurements over a period of 40 d (Supplementary Fig. 3). Dark release and photoinduced drug release were measured using dialysis membranes in phosphate-buffered saline at 37 °C with 10% fetal bovine serum added to each dialysis tube (Spectra/Por; NP[XL184], 100 kDa cutoff; PMILs, 300 kDa cut-off; Fig. 2f). A 690 nm diode laser (High Power Devices, Inc.) was used for all NIR irradiation experiments. During dialysis samples were collected periodically and placed immediately in acetonitrile containing 1% of the internal standard N-(1-naphthyl) ethylenediamine. Separation and quantification of drug components was achieved by liquid chromatography-tandem mass spectrometry (LC-MS/MS) using standard curves for each drug normalized to the internal standard. Briefly, 1.0 µl of dialysis sample was injected into a ZorbaxC18 (2.1 × 50 mm) column eluted at 0.400 ml min^{-1} with acetonitrile and 10 mM ammonium formate (80% → 20% over 4 min). Detection of drug components were made using triple quadrupole MS/MS detection with an ion source ESI+ in MRM scan mode to identify the product ions for BPD (ret. time = 4.12 min, 513 m/z) and XL184 (ret. time = 2.68 min, 232 m/z). Quantitative analysis of chromatograms allowed for area under curve integrations of each product ion normalized to the internal standard (ret. time 1.20 min; 170 m/z). Total moles were determined using standard curves and percent loss calculated for

each time point after correcting for sample volume changes. The resulting BPD and XL184 release profiles were fit individually to a simple one- or two-phase exponential model: $a_0 + a_1 \cdot e^{-k_1 \cdot t} + a_2 \cdot e^{-k_2 \cdot t}$, where a_0 is an offset, a_1 and a_2 are the Q6 maxima release plateaus (at equilibrium) of phases 1 and 2, k_1 and k_2 are the release rate constants of phases 1 and 2, and t is time from placing the sample in serum media within the dialysis tube. Note that XL184 release from NP[XL184] is sufficiently described by a single-phase model ($P=0.067$, two-phase alternative hypothesis), whereas XL184 release from the PMIL with or without laser irradiation is best described by the multi-phase model ($P =0.0003–0.0079$). Dynamic light scattering and transmission electron microscopy were also performed before and after photoirradiation (Fig. 3 and Supplementary Fig. 4).

Cryo-electron microscopy. Cryo-EM was performed using a FEI Technai G2 Polara microscope equipped with an energy filter (Gatan) and a K2 Summit direct detection device (Gatan). Briefly, 5 µl of nanomaterial sample (~60 µM BPD for the PMIL or L[BPD]; ~30 or 125 µM XL184 for the PMIL or NP[XL184], respectively) mixed with 2 µl of BSA Gold Tracer (EM-grade 6 nm; Electron Microscopy Sciences, 25484) re-suspended in phosphate-buffered saline were deposited onto glow-discharged holey carbon grids (QUANTIFOIL R 2/1 200 mesh, copper; Electron Microscopy Sciences), blotted and rapidly vitrified in a liquid ethane and propane mixture (50:50) using a custom-built plunger (Max Planck Institute of Biochemistry, Germany). Imaging was performed at 300 kV under low-dose conditions with 4.98 or 6.12 Å sampling and a defocus of −3 or −6 µm for 2D or 3D images, respectively. 2D images were obtained using the dose-fractionation mode of the detector (~20–40 e/Å^2 cumulative dose). Tilt series (±60°) for tomography were collected around a single axis with a 2° sampling increment using SerialEM software[47] (~100 e/Å^2 cumulative dose). Tomographic reconstructions were calculated using the IMOD tomography package[48]. Renders of 3D PMIL and NP[XL184] objects were created by manual segmentation in IMOD and rendered using VMD[49]. Manual particle counting was performed as described in Supplementary Fig. 5. Only unambiguous NP[XL184] objects were counted (~20 nm in diameter or greater). Mean lamellarity was calculated as: $\sum_L (N_L \cdot L)/\sum_L N_L$, where N_L is the number of objects with lamellarity L (for example, $L = 1$ for unilamellar liposomes).

Transmission electron microscopy. TEM (Philips CM10) was performed using negative staining either on untreated (200 mesh nickel PELCO Support Film with a Formvar/carbon coating, Ted Pella Inc.) or ionized carbon coated grids (to promote sample adhesion). Briefly, 10 µl of the sample was added to the grid, air-dried and stained (2 µl, 1.0% phosphotungstic acid). Next, the grid was blotted dry and washed with 5 µl–5 µl of dH$_2$O. Imaging was performed at 100.0 kV and magnifications of ~10,000–50,000×.

Cell culture studies. Monolayer cultures of AsPC1 cells (American Type Culture Collection, CRL-1682; low passage number, <20)—recently tested (July 2015) and found to be negative for mycoplasma contamination (MycoAlert mycoplasma detection kit, Lonza)—were maintained in media (RPMI 1640, Mediatech) supplemented with 10% fetal bovine serum (Invitrogen), 100 units per ml penicillin and 100 µg per ml streptomycin. The AsPC1 cell line has not been listed in the database of cross-contaminated or misidentified cell lines maintained by the International Cell Line Authentication Committee. Cellular uptake of PMILs and L[BPD] was tested in multi-well plates with coverslip bottoms (Greiner Bio-One) plated with AsPC1 cells allowed to attach and grow overnight. Nanoconstructs were added to the wells at staggered time points to reach a concentration of 100 nM BPD and to achieve varying incubation times at 37 °C (15–90 min). Imaging was performed with an Olympus FV1000 confocal microscope with a 20 × 0.75 NA (numerical aperture) objective. BPD excitation was performed using a 405 nm diode laser with an emission spectrograph centred on the 696 nm BPD fluorescence emission peak. The laser, photomultiplier tube detector and pinhole settings, as well as brightness–contrast adjustment settings for display, were kept constant for all images. In addition, phase contrast images were collected during microscopy to focus on a high-density field of cells (not shown). Images were also collected for untreated cells (0 min) to quantify the autofluorescence background and to define a fluorescence intensity threshold that rejects 99.5% of the background signal. This intensity threshold was applied to all images to select pixels above the autofluorescence background (true BPD signal) for analysis. The resulting cellular uptake data was fit to a simple biexponential pharmacokinetic model: $a \cdot (e^{-k \cdot t} - e^{-j \cdot t})$, where k and j are the elimination and absorption rate constants, a is a coefficient dependent on the administered BPD dose as well as its bioavailability and t is time post-administration. For in vitro PDT, $0.25 \cdot 10^6$ AsPC1 cells were grown on a 35-mm culture dish for 24 h and incubated with nanoconstructs containing BPD (250 nM equivalent) and/or XL184 (100–125 nM equivalent) in 1 ml complete medium for 1 h. The incubation media was then replaced with 2 ml of fresh, complete media before photoirradiation. This removal of nanoconstructs not uptaken by cells before irradiation limits the release of XL184 and the generation of photocytotoxic species to intracellular and cell-associated nanoconstructs. Cell viability was measured using the MTT assay 24 h following light irradiation. Singlet Oxygen Sensor Green (SOSG; Molecular Probes) and D-mannitol (Sigma-Aldrich) were used to probe reactive oxygen species involvement in BPD-PDT-induce MET activation. Tyrphostin AG1478 (Sigma-Aldrich) and bacterial toxin B (Toxin B, *Clostridium*

difficile - Calbiochem, Millipore) were used to test for the involvement of enzymes known to participate in MET transactivation. SOSG and mannitol were added to cells immediately before laser irradiation in fresh media and then removed immediately after PDT by a second media replacement step. AG1478 and toxin B were incubated with cells in fresh media for 30 min and 2 h, respectively, before laser irradiation and then removed immediately after PDT by a second media replacement.

***In vivo* mouse models and treatments.** All animal experiments were conducted with approval and according to guidelines established by the Massachusetts General Hospital Institutional Animal Care and Use Committee. Experiments were carried out on 6-week-old male Swiss nude mice weighing 20–25 grams (Cox Breeding Laboratories). For tumour implantations and photoirradiation, animals were anesthetized with 84 mg kg^{-1} ketamine and 12 mg kg^{-1} xylazine. Tumours were implanted by injection of a 50 μl volume containing 10^6 AsPC1 cells in a 1:1 mixture of Matrigel (BD Biosciences) and culture media. Subcutaneous tumours were implanted above the hind leg and tumour volumes were estimated longitudinally by measuring the three tumour dimensions using a calliper and the hemi-ellipsoid formula: volume = $\pi \cdot L \cdot W \cdot H/6$, where L, W and H, are the tumour length, width and height. Note that here, H, represents the measured height of the hemi-elliptical tumour, which is half the height of a full ellipsoid. Eighteen days following cancer cell implantation, subcutaneous tumours reached volumes of ~50 mm^3 prior to the start of treatment. For orthotopic tumour implantation, animals were laid supine, a small left abdominal flank incision was made to exteriorize the pancreas and the cell suspension was injected into the pancreas. A small amount of 10% povidone/iodine was applied topically to the injection site. Then the incision was closed with 4–0 sutures and 10% povidone/iodine was then applied to the incision site to prevent infection. Ten days after cancer cell implantation, orthotopic pancreatic tumours reached volumes of ~25 mm^3 before the start of treatment. All injections for treatment were done intravenously (tail vein) in 200 μl sterile phosphate-buffered saline. Mice were randomized into the various treatment groups, and the tumours of mice receiving BPD were irradiated with NIR light (using the 690 nm diode laser listed above) 1 h post-injection, delivered at an irradiance of 100 mW cm^{-2}. Subcutaneous tumours were irradiated transcutaneously whereas orthotopic tumours were surgically exposed as for tumour implantation and irradiated. Fourteen days after treatment, orthotopic tumours were excised to estimate their volumes using callipers and the ellipsoid formula above.

Microvessel immunofluorescence imaging. Microvessel density and intratumoural microvessel volume were estimated as described previously[38]. Briefly, orthotopic pancreatic tumours were excised 2 weeks post-treatment, embedded in optimal cutting temperature compound and frozen at −80 °C. A cryotome was used to cut 20-μm-thick cryosections. Sections were (1) fixed in 1:1 acetone:methanol for 15 min at −20 °C, (2) air dried for 30 min, and (3) washed three times in phosphate-buffered saline. A blocking solution (Dako Protein Block Reagent) was applied for 30 min, followed by application of the immunostains, at ~5 μg ml monoclonal antibody (MAb) each diluted in background reducing Dako Antibody Diluent for 2 h at room temperature in a humidifying chamber. Finally, the slides were washed again three times, mounted (Invitrogen SlowFade Gold with 4′,6-diamidino-2-phenylindole, DAPI) with a coverslip and sealed with nail polish. Confocal fluorescence imaging was performed using an Olympus FluoView 1,000 confocal microscope with a 10 × 0.4 numerical aperture (NA) or a 20 × 0.75 NA objective. Excitation of DAPI, anti-mouse PECAM-1 (CD31; clone 390; CBL1337, Millipore) MAb-Alexa Fluor 568 conjugates and anti-human cytokeratin 8 (clone LP3 K; MAB3156, R&D Systems) MAb-Alexa Fluor 647 conjugates was carried out using 405-, 559- and 635-nm lasers, respectively. Mosaic images of entire tumour cross-sections were collected and stitched together using the Olympus FluoView software. The anti-human cytokeratin 8 stain (a cytoskeletal protein highly expressed by AsPC1 cells) has dual selectivity for the epithelial cancer cells because it does not react with mouse proteins. All analyses were performed using custom MATLAB (Mathworks) routines for batch image processing[38]. Microvessel density values were calculated from whole tumour sections, within viable tumour tissue only, and averaged over slices from the entire tumour rather than a more complex 'hot spot'

identification and calculation, which is difficult to define objectively[38]. Intratumoural microvessel volume is calculated by multiplying microvessel density with the viable tumour volume in each slice and then summing over the whole tumour by interpolation[38]. Here, we used the minimum tumour subsampling necessary—based on a mathematical model—to resolve a statistically significant change in intratumoural microvessel volume, as validated previously using the orthotopic AsPC1 tumour model[38] (Supplementary Note 9).

Measurement of metastatic burden. A quantitative reverse transcription–polymerase chain reaction (qRT-PCR) assay was performed on excised liver and iliac lymph nodes to estimate the number of human cancer cells in excised organs as described and validated previously[44]. Briefly, qRT-PCR is used to measure the total number of human cancer cells from the level of human and mouse glyceraldehyde 3-phosphate dehydrogenase (GAPDH) housekeeping genes. At least 300 mg of freshly excised liver and retroperitoneal lymph nodes were collected at the treatment endpoint and snap frozen in liquid nitrogen. The frozen samples were then pulverized and homogenized, followed by RNA extraction (RNAeasy Plus Mini Kit; Qiagen). Human and mouse GAPDH gene were measured using custom synthesized primers (Invitrogen). For each specimen, the cycle threshold (C_t) from human GAPDH gene was normalized by C_t from mouse GAPDH gene. The normalized C_t was quantified into number of cancer cells using a standard curve generated with a set of organ lysates from no-tumour control mice mixed with different numbers of human cancer cells.

Statistical analyses. Specific statistical tests are indicated in the figure captions and were carried out using GraphPad Prism (GraphPad Software). All reported P values are two-tailed. Parametric tests (one-way ANOVA with Tukey's *post hoc* test) were used for *in vitro* drug release (Fig. 2f and Supplementary Fig. 4) and *in vitro* cell culture (Fig. 4b,c,d and Supplementary Fig. 6) studies; and, the D'Agostino & Pearson omnibus normality test ($\alpha = 0.05$; requires $n \geq 8$ replicates per group) did not identify significant deviations from normality within these data sets (testing could only performed for groups with $n \geq 8$ replicates). Note that all groups within the drug release data were analysed together (some groups appear only in Supplementary Fig. 4). Electron microscopy single-nanoparticle analysis (Fig. 3d) and all *in vivo* data (Figs. 5b,c,d, 6b,c,d and Supplementary Fig. 1) were analysed using nonparametric tests (the Mann-Whitney U test or Kruskal–Wallis one-way ANOVA). The Brown–Forsythe test ($\alpha = 0.05$) was applied to all data sets with $n \geq 3$ replicates to test for equal variance (regardless of whether parametric or nonparametric analysis was used) and identified significant deviations from equal variance (Figs. 3e, 5d and 6c). In these cases, the data were analysed following a logarithmic transform of the data to pass the Brown–Forsythe test. Two-way ANOVA was applied to test for synergistic treatment interactions[50] (Fig. 5d) following a natural logarithm transform of the data to pass the D'Agostino & Pearson omnibus normality test. No exclusion criteria were used, and no data points or animals were excluded from analysis. Investigators were not blinded to experimental groups unless noted otherwise. Animal sample sizes were selected to ensure adequate power (80%) to detect a 20% difference using a maximum of 16 animals per group assuming a standard deviation of 15%. For the subcutaneous model, significance was achieved with 5 animals per group.

References

45. Cheng, J. *et al.* Formulation of functionalized PLGA–PEG nanoparticles for in vivo targeted drug delivery. *Biomaterials* **28,** 869–876 (2007).
46. Nel, A. E. *et al.* Understanding biophysicochemical interactions at the nano–bio interface. *Nature Mater.* **8,** 543–557 (2009).
47. Mastronarde, D. N. Automated electron microscope tomography using robust prediction of specimen movements. *J. Struct. Biol.* **152,** 36–51 (2005).
48. Kremer, J. R., Mastronarde, D. N. & McIntosh, J. R. Computer visualization of three-dimensional image data using IMOD. *J. Struct. Biol.* **116,** 71–76 (1996).
49. Humphrey, W., Dalke, A. & Schulten, K. VMD: visual molecular dynamics. *J. Mol. Graphics* **14,** 33–38 (1996).
50. Larson, M. G. Analysis of variance. *Circulation* **117,** 115–121 (2008).

Query no.	Query	Response
Q1	Please note it is against style to use author's names when citing references in the text, all cases have been reworded.	
Q2	The figure captions have been adjusted for style, please check all panel descriptions are accurate.	
Q3	In Fig. 3, please add the correct label for each of the images in panel a (NP[XL184], L[BPD] OR PMIL).	
Q4	Please note that names in the Acknowledgements section have been adjusted for style.	
Q5	Please define T_m in the methods.	
Q6	Is the centre dot in equations in the Methods used to denote multiplication? If so, it will be replaced for style.	
Q7	Please check the heading levels in the Methods section and adjust as needed.	